HHS Public Access

Author manuscript

Invest Radiol. Author manuscript; available in PMC 2019 November 01.

Published in final edited form as:

Invest Radiol. 2018 November ; 53(11): 655–662. doi:10.1097/RLI.0000000000000488.

150 Micron Spatial Resolution using Photon Counting Detector CT Technology: Technical Performance and First Patient Images

Shuai Leng, PhD[1], **Kishore Rajendran, PhD**[1], **Hao Gong, PhD**[1], **Wei Zhou, PhD**[1], **Ahmed F. Halaweish, PhD**[2], **Andre Henning, PhD**[3], **Steffen Kappler, PhD**[3], **Matthias Baer, PhD**[3], **Joel G. Fletcher, MD**[1], and **Cynthia H. McCollough, PhD**[1,*]

[1]Department of Radiology, Mayo Clinic, Rochester, MN

[2]Siemens Healthcare, Malvern, PA

[3]Siemens Healthcare, Forchheim, Germany

Abstract

Objective—To quantitatively assess two new scan modes on a photon-counting detector (PCD) CT system, each designed to maximize spatial resolution, and to qualitatively demonstrate potential clinical impact using patient data.

Materials and Methods—This HIPAA-compliant study was approved by our institutional review board. Two high-spatial-resolution scan modes (*Sharp* and *UHR*) were evaluated using phantoms to quantify spatial resolution and image noise, and results were compared to the standard mode (*Macro*). Patients were scanned using a conventional energy-integrating-detector (EID) scanner and the PCD scanner using the same radiation dose. In first patient images, anatomic details were qualitatively evaluated to demonstrate potential clinical impact.

Results—*Sharp* and *UHR* modes had a 69% and 87% improvement in in-plane spatial resolution, respectively, compared to *Macro* mode (10% MTF values of 16.05, 17.69, and 9.48 lp/cm, respectively). The cut-off spatial frequency of the *UHR* mode (32.4 lp/cm) corresponded to a limiting spatial resolution of 150 microns. The full-width-at-half-maximum values of the section sensitivity profiles were 0.41, 0.44 and 0.67 mm for the thinnest image thickness for each mode (0.25, 0.25 and 0.5 mm, respectively). At the same in-plane spatial resolution, *Sharp* and *UHR* images had up to 25% lower noise than *Macro* images. Patient images acquired in *Sharp* mode demonstrated better delineation of fine anatomic structures compared to *Macro* mode images.

Conclusions—Phantom studies demonstrated superior resolution and noise properties for the *Sharp* and *UHR* modes relative to the standard *Macro* mode and patient images demonstrated the potential benefit of these scan modes for clinical practice.

Keywords

Computed tomography (CT); photon counting detector (PCD); high spatial resolution; dual energy

[*]**Corresponding Author**. 200 First Street SW, Rochester, MN 55905, Phone: (507) 284-2511, Fax: (507) 266-0631, mccollough.cynthia@mayo.edu.

INTRODUCTION

Recently, photon-counting detector (PCD) technology has been introduced into X-ray CT imaging [1–8]. Different from the conventional energy-integrating detectors (EIDs) used in commercial CT systems, X-ray photons directly produce electric signals in PCDs where the amplitude of the signal is related to the energy of the detected photon. PCDs count individual photons and allocate each count into distinct energy bins, according to the measured photon energy. Compared to EID-CT systems, PCD-CT systems offer lower electronic noise, improved CT number accuracy, and higher contrast-to-noise ratio (CNR), which provides higher dose efficiency for contrast-enhanced CT [1–3, 5–7, 9–14]. Further, the energy discriminating nature of PCD-CT enables multi-energy CT, with 2 or more energy bins, which may lead to new clinical applications, such as simultaneous imaging of multiple contrast agents and functional imaging using nanoparticles [5, 15–18].

A whole-body PCD-CT was built and made available for investigational studies at our institution.[7, 16, 19–21]. Phantom, animal and cadaver studies at clinical dose levels and dose rates have demonstrated that the PCD-CT provides equivalent or improved image quality compared to EID-CT, but with higher iodine CNR, lower electronic noise and reduced beam-hardening artifacts [12, 19, 22]. Human studies of the abdomen, and head and neck, have validated non-inferior performance of PCD-CT compared to EID-CT [23, 24].

In EIDs, X-ray photons interact with a scintillator material to generate visible light, which is consequently detected by a photodiode to produce electric signals. EIDs require septa between individual detector cells to prevent this light from spreading across detector boundaries. The septa reduce dose efficiency as they cause “dead space” on the detector surface. PCD’s direct-conversion technique avoids the intermediate step of creating visible light; therefore reflective septa between detector cells are not required. This allows use of smaller detector cells in PCDs without sacrificing dose efficiency. A scanning technique using 0.25 mm × 0.25 mm detector cells (at isocenter) on the PCD-CT was recently reported, with both phantom and cadaveric studies demonstrating potential clinical benefit for the PCD technique compared to EID-CT [25]. The technique was only available in service mode without table translation. In addition, the mode was limited to one energy threshold, which did not allow the simultaneous acquisition of multi-energy CT data, which is one of the major benefits of PCD-CT. These two limitations prevented the mode from being used for human studies. In 2016, two new “clinical” high-spatial-resolution scan modes, each having multi-energy capabilities, were introduced on the research PCD-CT scanner [26, 27]. To our knowledge, the evaluation of simultaneous high-resolution and multi-energy capabilities of PCD-CT of patients using the high-resolution modes has not been reported. The purpose of this study was to quantitatively assess the two high-spatial-resolution scan modes and to qualitatively demonstrate potential clinical impact using first patient scans.

MATERIALS AND METHODS

This prospective, HIPAA-compliant study was approved by our institutional review board, with written informed consent obtained from each participant.

PCD-CT Scanner and High-Spatial-Resolution Scan Modes

The PCD-CT scanner used is a modified 2nd-generation dual-source CT scanner (SOMATOM Definition Flash, Siemens Healthcare), with one of the two EID subsystems replaced by a PCD subsystem. The scan field-of-view (FOV) of the EID and PCD subsystems are 50 and 27.5 cm, respectively. A data-completion scan using the EID subsystem is required for PCD exams of subjects whose width exceeds 27.5 cm FOV to avoid data truncation artifact [28]. The PCD subsystem is capable of acquiring energy-selective data with either 2 or 4 energy thresholds. Details of the scanner have been described elsewhere [7, 12, 16, 19–21].

The native detector pixel of the PCD is 0.225 mm × 0.225 mm (at the detector plane), however, the standard readout, referred to as *Macro* mode, groups 4 × 4 native detector pixels to form an effective detector pixel of 0.9 × 0.9 mm (Figure 1). Given the system's magnification of 1.8, this results in a 0.5 mm × 0.5 mm detector pixel size at isocenter. Two energy thresholds are available in this mode. Another mode, referred to as *Chess* mode, has the same detector size as the *Macro* mode but interlaced subpixels are operated at different energy thresholds, resulting in 4 energy thresholds for this mode. The z-axis collimation is 32 × 0.5 mm (16 mm coverage) for both *Macro* and *Chess* modes (Figure 1) [7, 19]. Since spatial resolution is the same between *Macro* and *Chess* mode, in this study we only used *Macro* mode for comparison with the new high-spatial-resolution scan modes.

The two new high-spatial-resolution scan modes, namely *Sharp* and *UHR* modes, both have 2 energy thresholds (Figure 1) [29]. In *UHR* mode, low- and high-energy thresholds have the same detector pixel size of 0.25 mm × 0.25 mm (at isocenter). The z-axis collimation is reduced to 32 × 0.25 mm (8 mm coverage, Figure 1) to handle the increase in generated data (4 times more than *Macro* mode) without exceeding data transfer limits. A rotation time of 1 second is available. The focal spot size is 0.7 mm × 0.7 mm and tube power is limited to 48 kW. In *Sharp* mode, to increase the detector coverage and scan speed, the low-energy threshold data maintains the same detector pixel size as the *UHR* mode (0.25 mm × 0.25 mm), while the high-energy threshold data uses a 0.5 mm × 0.5 mm detector pixel, which allows an increase in collimation to 48 × 0.25 mm (12 mm coverage, Figure 1). Two rotation time options are available, 0.5 and 1 second. The *Sharp* mode uses a larger focal spot (0.9 mm × 1.1 mm) and higher tube power (100 kW) limit than the *UHR* mode. The focal spot size is determined by the scan mode and not selectable by the user.

Phantom Experiments to Assess Spatial Resolution and Image Noise

Spatial resolution was quantitatively assessed using the modulation-translation-function (MTF) in the axial plane and section-sensitivity-profile (SSP) along the longitudinal (z) direction for *Macro*, *Sharp* and *UHR* modes. A 50 μm diameter tungsten wire was placed in a solid water phantom and scanned with the wire parallel to the z-axis of the scanner. All scans were performed in spiral mode, with 0.5 second rotation time, 140 kV and energy thresholds of 25 and 75 keV. Full spectrum (low energy threshold) images were reconstructed using weighted filtered-backprojection (FBP) [30] and the smallest FOV (50 mm), a 1024×1024 image matrix, and 0.75 mm image thickness. Reconstruction was performed using two kernels: B70 (the preferred high resolution kernel in our practice for

most applications) and S80 (Shepp-Logan kernel designed to reproduce the maximal system frequency that the hardware is capable of). The point spread function was obtained from the reconstructed images of the wire, MTF curves were calculated, and the MTF values at 10% and 0% were recorded. SSPs were measured using a 25 μm thick gold foil embedded in a Lucite cylinder (QRM, GmbH, Moehrendorf, Germany), which was scanned with the foil perpendicular to the z-axis of the scanner. Images were reconstructed with 75 mm FOV, a 1024×1024 image matrix, and a S80 kernel. Images were reconstructed at the narrowest image thickness for each mode, i.e. 0.5, 0.25 and 0.25 mm for *Macro*, *Sharp* and *UHR* modes, respectively. For noise comparisons, images were also reconstructed at 0.5 mm for *Sharp* and *UHR* modes, the same thickness as used by the *Macro* mode. The smallest reconstruction increment allowed (0.05 mm) was used to provide sufficient sampling of the SSP along the z-axis. SSPs were plotted and the full-width-at-half-maximum (FWHM) values were calculated.

Image noise in the low-energy threshold images was measured by scanning an anthropomorphic head phantom using *Macro* and *Sharp* modes at matched tube-current-time-product levels (150 mAs, $CTDI_{VOL}$ = 38 mGy) as used in our clinical practice.. Images were reconstructed with identical parameters for all modes: 1.0 mm image thickness, 275 mm FOV, 1024 × 1024 matrix, and a sharp kernel (H70), which is the bone kernel used for routine head CT scans at our institution. Noise was measured as the standard deviation of CT numbers inside a circular region of interest (ROI) drawn in a uniform area of the images.

First Patient Images and Qualitative Demonstration of Potential Clinical Impact

Adult subjects referred for clinically-indicated CT exams were recruited to participate in this study, which involved a research PCD-CT scan of the same anatomy as was imaged clinically. After obtaining written informed consent, patients were scanned on the PCD-CT for the same indication as the clinical exam and with the same radiation dose ($CTDI_{VOL}$).

CT exams of the shoulder, lung, abdomen, head and temporal bone were included in this proof-of-principle study. All clinical exams were performed using standard clinical protocols on a 128-slice CT scanner (SOMATOM Definition Edge or SOMATOM Definition Flash, Siemens Healthcare; these systems are identical when operated in the single energy mode, which was the case for these exams). The temporal bone scan was performed with an ultra-high spatial resolution mode using a comb filter along the fan-angle direction to reduce effective detector pixel size [31–33]. All research exams were performed on the PCD-CT using either *Sharp* or *UHR* mode, 140 kV, 25 and 75 keV energy thresholds, and $CTDI_{VOL}$ matched to that of the clinical EID-CT exam. The tube potential and energy thresholds were chosen to achieve a balance between energy separation and the number of photons in each energy bin, which determines the noise in each bin image. Images were reconstructed with identical parameters (kernels, image thickness and increment) for the clinical and research scans of each patient. Specific scanning and reconstruction parameters are summarized in Table 1.

Simultaneous High Spatial Resolution and Multi-Energy Capabilities

To demonstrate the ability of the *Sharp* and *UHR* modes to simultaneously acquire high spatial resolution and multi-energy images, multi-energy data processing was performed for a contrast-enhanced head exam (CT angiography, CTA), and a renal stone exam. The head CTA exam used 50 mL of contrast media (Omnipaque 350, GE Healthcare) In addition to the high-spatial-resolution low-energy threshold images reconstructed with a sharp kernel, both the low- and high-energy threshold data were reconstructed with a weighted filtered back projection algorithm using a quantitative soft kernel (D30) and processed for dual-energy analysis on prototype software provided by the manufacturer (eXamine, Siemens Healthcare). Bone removal was performed for the head CTA case, and stone composition analysis was performed for the renal stone exam, where uric acid (UA) and non-uric acid (NUA) components were color-coded as red and blue, respectively. See Table 1 for additional image reconstruction parameters.

RESULTS

Spatial Resolution and Image Noise

With B70, which was designed to convey nearly the best achievable resolution given the detector pixel size of the EID-CT system, all three modes demonstrated similar MTF curves, with 10% MTF values corresponding to 9.91, 9.99 and 9.97 lp/cm for *Macro*, *Sharp* and *UHR*, respectively (Figure 2a). For S80, which was designed to convey the best achievable resolution given the detector pixel size of the PCD-CT system, *Sharp* and *UHR* modes showed similar MTFs, both better than for *Macro* mode, with 10% MTF values corresponding to 9.48, 16.05, 17.69 lp/cm for *Macro*, *Sharp* and *UHR*, respectively (Figure 2b). It should be noted that the *UHR* and *Sharp* mode demonstrated similar MTF values in the low threshold images due to the identical detector pixels sizes in these modes. With S80, the cut-off spatial frequency of the *UHR* mode (32.4 lp/cm) corresponded to a limiting spatial resolution of 150 microns. The SSPs for *Macro*, *Sharp* and *UHR* images reconstructed at the thinnest slice thickness possible, i.e. 0.5, 0.25 and 0.25 mm, respectively, demonstrated that *UHR* mode had the narrowest SSP (0.41 mm), followed by *Sharp* mode (0.44 mm) and *Macro* mode (0.67 mm) (Figure 3). For the same reconstructed image thickness of 0.5 mm, *Sharp* and *UHR* modes had narrower SSPs (0.57 and 0.58 mm) than *Macro* mode (0.67 mm). The similarity in the SSPs between *Sharp* and *UHR* modes can be attributed to the identical detector pixel sizes used in these acquisition modes for low-energy threshold images.

Images of the anthropomorphic head phantom scanned with *Macro* and *Sharp* modes and reconstructed with the same head kernel (Figure 4) demonstrated that the low-energy threshold images acquired with *Macro* mode were noisier than *Sharp* mode for the same kernel (i.e., the same in plane spatial resolution). ROI measurements showed a 15% noise reduction for *Sharp* mode compared to *Macro* mode.

First Patient Images and Qualitative Demonstration of Potential Clinical Impact

For lung images of the same patient scanned on a commercial EID scanner and the PCD-CT (Figure 5), the PCD-CT image was visibly sharper than the EID-CT image. More small

vessels were observed in the PCD-CT image compared to that from the EID scanner. In addition, excellent delineation of the airway walls was achieved with PCD-CT, which was challenging in the EID-CT images. Shoulder images of the same patient (Figure 6) demonstrated sharper cortex and trabeculae bones, and subchondral cysts and sclerosis, with PCD-CT compared to EID-CT. Temporal bone images of the same patient scanned on an EID-CT using a comb filter and the PCD-CT using *UHR* mode (Figure 7) showed similar image sharpness, with both clearly delineating the incudomallear joint. However, ROI measurements showed 21% lower image noise for PCD-CT images (112 HU) than EID-CT (141 HU) images.

Simultaneous High Spatial Resolution and Multi-Energy Capabilities

A *Sharp* mode, low-energy threshold image of the head CTA exam shows clear delineation of fine blood vessels, soft tissue and bony structures (Figure 8a). This image can be used for standard diagnostic tasks. Because both low- and high-energy data were acquired simultaneously, dual-energy post-processing could be performed to remove bony anatomy (Figure 8b).

The low-energy threshold *Sharp* mode images from the renal stone exam with 0.25 mm image thickness demonstrated sharp boundaries of the stone, as well as two distinct regions of one stone: the darker core of the stone surrounded by a thin brighter shell (Figure 9a). Dual-energy analysis demonstrated the mixed composition of this stone, which had both uric acid (red) and non-uric-acid (blue) components (Figure 9b). The other stone was rather uniform in the low-energy threshold image and dual-energy analysis showed a pure uric acid (red) stone.

DISCUSSION

In this study, two high spatial-resolution, multi-energy scan modes on a PCD-CT scanner, with a detector pixel size of 0.25 mm at the isocenter, were described. MTF measurements demonstrated strong dependence of spatial resolution on reconstruction kernel: spatial resolution was the same for all modes when images were reconstructed with a conventional sharp kernel (B70); while *Sharp* and *UHR* modes had much higher spatial resolution than *Macro* mode when a Shepp-Logan kernel (S80) was used. This was due to the fact that Shepp-Logan kernel was designed to convey the highest possible spatial frequency achievable by each system, while the B70 kernel was designed to produce identical image sharpness, regardless of the detector pixel size. As *Sharp* and *UHR* modes had smaller detector pixels than *Macro* mode, the resolution benefits were fully demonstrated using the Shepp-Logan kernel (S80). When spatial resolution was matched, benefit was still achieved with the *Sharp* and *UHR* modes, in the form of lower image noise. This is due to the fact that *Sharp* and *UHR* modes have a better intrinsic MTF due to the smaller detector size. Therefore, a more aggressive smoothing filter can be applied to the *Sharp* and *UHR* data compared to the *Macro* mode while achieving the same MTF in the final images, as demonstrated with simulations in a previous study [34]. This is possible because identical kernels require only identical MTF values; the actual smoothing filter used to achieve the specified MTF can be stronger, and hence reduce the image noise to a greater extent.

Along the z-axis, *Sharp* and *UHR* modes have nominal images thicknesses of 0.25 mm, which is half that of *Macro* mode. Phantom studies confirmed narrower SSPs for *Sharp* and *UHR* modes compared to *Macro* mode. Comparing *Sharp* and *UHR* modes, although both have the same nominal slice thickness of 0.25 mm, *UHR* mode showed a slightly narrower SSP than *Sharp* mode due to the smaller focal spot size of *UHR* mode (0.7 mm × 0.7 mm) than *Sharp* mode (0.9 mm × 1.1 mm).

Spatial resolution in CT plays a critical role in clinical diagnosis. Different methods have been investigated to increase spatial resolution. One example is the use of post-patient comb filters to reduce effective detector size. However, this method comes with reduced dose efficiency as the blocked photons have already contributed to patient dose, but do not contribute to the reconstructed image [31]. As shown in the temporal bone images, at matched radiation dose, image noise was higher using the EID and comb filter compared to that of the *UHR* mode in PCD-CT. Because of the reduced dose efficiency, the comb filter is only available in head and extremity exams, but not for body exams. The introduction of *Sharp* and *UHR* modes in PCD-CT, which allow improved spatial resolution without loss of dose efficiency, makes it possible to offer improved spatial resolution for imaging of any part of the body. Unlike high-spatial-resolution modes offered with smaller EID detectors, the loss of geometric efficiency from an increased density of septa is not an issue for PCD-CT [35]. This may allow visualization of small structures that were not visible before, enabling new applications in the torso. In the sample exams shown in this study, improved spatial resolution and better delineation of fine anatomic structures was demonstrated compared to EID scanners. In addition, the energy discriminating nature of the PCD enables simultaneous acquisition of high-spatial-resolution and multi-energy CT data (unlike current dual-energy systems equipped with the UHR comb filter, which can scan in either dual-energy or UHR modes, but not both simultaneously). Examples in musculoskeletal and renal stone imaging showed the ability of PCD-CT to provide both benefits using a single scan. These initial results are encouraging and warrant future studies for quantitative evaluation of the clinical benefit derived from use of these scan modes. In conventional EID CT, septa are used to reduce cross-talk between detectors; however they also reduce geometric efficiency (fill factor). In PCD, the absence of septa improves geometric efficiency; however, their absence allows for detector cross-talk, such as charge sharing. For the research PCD-CT system investigated in this study, the anti-scatter grid is aligned with the Macro pixels; there is no anti-scatter grid aligned with the smaller pixels of the *Sharp* and *UHR* mode, which may allow for more detected scatter in these modes.

To accommodate the improved spatial resolution of the *Sharp* and *UHR* modes, image voxel size needs to be small enough to avoid stair-step artifacts and pixelation. A 512 × 512 image matrix is not sufficient for conveying the maximum spatial resolution for a large FOV (275 mm) reconstruction. Although reducing reconstruction FOV can effectively reduce voxel size, it is inconvenient in some scenarios (e.g., where bilateral anatomy is desired to be viewed in a single image) and inadequate in other scenarios, where full FOV is required (e.g., lung imaging). A 1024 × 1024 image matrix supports use of full FOV images with the maximum achievable spatial resolution. This requires that informatics systems, such as PACS and post-processing workstations, be able to accept and process 1024 × 1024 images.

In this study, the simultaneous high-resolution and dual-energy capabilities were investigated using Sharp mode instead of UHR mode. The main difference between Sharp mode and UHR mode is the resolution of the high-energy threshold images. Different from standard diagnostic tasks, which can substantially benefit from the ultra-high resolution, standard resolution low- and high-energy images (with 0.5 mm thickness) are sufficient for material quantification in dual-energy applications. This is because the material decomposition process tends to amplify image noise, limiting the benefit from use of a smaller detector size for the material decomposition process [26]. Sharp mode, which yields ultra-high resolution in the low-energy threshold image and regular (macro) resolution in dual-energy images, represents a flexible imaging mode that can provide both ultra-high resolution images and dual-energy capabilities. In addition, Sharp mode has 50% wider collimation, therefore a faster scanning speed, compared to UHR mode. Due to these reasons, Sharp mode has been used in this study for dual-energy investigations.

In this study, when comparing the performance of EID to PCD, $CTDI_{vol}$ was matched by adjusting the tube current accordingly. This was done intentionally, as we desired to compare image quality at the same patient dose. Because the PCD system used a narrower collimation than did the EID system, the $CTDI_{vol}$ per tube-current-time-product (mAs) was higher on the PCD-CT system than on the EID CT system. Thus, the same $CTDI_{vol}$ was achieved by using a lower tube current on the PCD system; use of the same tube-current would have led to use of higher dose on the PCD-CT system, giving it an unfair noise advantage over the EID CT system. The narrower collimation (and hence higher patient dose per mAs) is a property of the specific research PCD-CT system; it is not an intrinsic limitation of the PCD technology. Reduced coverage in the high-resolution modes compared to Macro mode was mainly due to design constraints in the electronic data readout, which was initially designed for the Macro and Chess acquisition modes. Greater z coverage could be achieved for a future PCD-CT system by designing appropriate readout electronics to handle the high data throughput of a PCD array without compromising z-coverage. Thus, the benefits observed in this study could be even stronger if a wider collimation PCD array becomes available in the future.

There were some limitations to this study, primarily in that image quality and potential diagnostic value were only qualitatively assessed for a few patient cases. The examples shown were included for the purpose of demonstrating the appearance of the improved spatial resolution using human anatomy, and to provide a hint of the potential clinical value, which would be difficult to do using only phantoms. Future work to quantify clinical impact is clearly needed; such studies are underway at our center.

In conclusion, the *Sharp* and *UHR* high-spatial-resolution, multi-energy scan modes on a whole-body PCD-CT scanner demonstrated a 69% and 87% improvement in in-plane spatial resolution, respectively, compared to relative to the originally released *Macro* acquisition mode. The maximum resolution of 150 microns provides an unprecedented opportunity to explore new clinical applications and to faithfully reproduce finer structures than have been previously possible. First human subject studies qualitatively demonstrated the improvement in anatomic visualization made possible by these new modes.

Acknowledgments

The project described was supported by the National Institutes of Health under award numbers R01 EB016966 and C06 RR018898 and in collaboration with Siemens Healthcare. The content is solely the responsibility of the authors and does not necessarily represent the official views of the National Institute of Health. The device described is a research scanner and not commercially available.

References

1. Taguchi K, Iwanczyk JS. Vision 20/20: Single photon counting x-ray detectors in medical imaging. Med Phys. 2013; 40(10):100901. [PubMed: 24089889]
2. Tümer T, et al. Preliminary results obtained from a novel CdZnTe pad detector and readout ASIC developed for an automatic baggage inspection system. Nuclear Science Symposium Conference Record. 2000; 1:4/36–4/41.
3. Shikhaliev PM. Energy-resolved computed tomography: first experimental results. Phys Med Biol. 2008; 53(20):5595–613. [PubMed: 18799830]
4. Shikhaliev PM, Fritz SG. Photon counting spectral CT versus conventional CT: comparative evaluation for breast imaging application. Phys Med Biol. 2011; 56(7):1905–30. [PubMed: 21364268]
5. Schlomka JP, et al. Experimental feasibility of multi-energy photon-counting K-edge imaging in pre-clinical computed tomography. Phys Med Biol. 2008; 53(15):4031–47. [PubMed: 18612175]
6. Iwanczyk JS, et al. Photon counting energy dispersive detector arrays for x-ray imaging. IEEE transactions on bio-medical engineering. 2009; 56(3):535–542.
7. Kappler S, et al. A research prototype system for quantum-counting clinical CT. Proceedings of SPIE--the International Society for Optical Engineering. 2010; 7622:76221Z.
8. Butler A, et al. Bio-medical X-ray imaging with spectroscopic pixel detectors. Nuclear Instruments and Methods in Physics Research Section A: Accelerators, Spectrometers, Detectors and Associated Equipment. 2008; 591(1):141–146.
9. Shikhaliev PM. Computed tomography with energy-resolved detection: a feasibility study. Phys Med Biol. 2008; 53(5):1475–95. [PubMed: 18296774]
10. Persson M, et al. Energy-resolved CT imaging with a photon-counting silicon-strip detector. Physics in medicine and biology. 2014; 59(22):6709–27. [PubMed: 25327497]
11. Bennett JR, et al. Hybrid spectral micro-CT: system design, implementation, and preliminary results. IEEE transactions on bio-medical engineering. 2014; 61(2):246–53. [PubMed: 23996533]
12. Gutjahr R, et al. Human Imaging With Photon Counting-Based Computed Tomography at Clinical Dose Levels: Contrast-to-Noise Ratio and Cadaver Studies. Investigative radiology. 2016
13. Symons R, et al. Low-dose lung cancer screening with photon-counting CT: a feasibility study. Physics in medicine and biology. 2016; 62(1):202. [PubMed: 27991453]
14. Schmidt TG, Zimmerman KC, Sidky EY. The effects of extending the spectral information acquired by a photon-counting detector for spectral CT. Physics in medicine and biology. 2015; 60(4):1583. [PubMed: 25615511]
15. Roessl E, Proksa R. K-edge imaging in x-ray computed tomography using multi-bin photon counting detectors. Phys Med Biol. 2007; 52(15):4679–96. [PubMed: 17634657]
16. Kappler S, et al. Photon counting CT at elevated X-ray tube currents: contrast stability, image noise and multi-energy performance. Proceedings of SPIE--the International Society for Optical Engineering. 2014; 9033:90331C.
17. Li Z, et al. Image-based Material Decomposition with a General Volume Constraint for Photon-Counting CT. Proceedings of SPIE--the International Society for Optical Engineering. 2015; 9412:94120T.
18. Faby S, et al. Performance of today's dual energy CT and future multi energy CT in virtual non-contrast imaging and in iodine quantification: A simulation study. Med Phys. 2015; 42(7):4349–4366. [PubMed: 26133632]

19. Yu Z, et al. Evaluation of conventional imaging performance in a research whole-body CT system with a photon-counting detector array. Physics in medicine and biology. 2016; 61(4):1572–95. [PubMed: 26835839]
20. Kappler S, et al. First results from a hybrid prototype CT scanner for exploring benefits of quantum-counting in clinical CT. Proceedings of SPIE--the International Society for Optical Engineering. 2012; 8313:83130X.
21. Kappler S, et al. Multi-energy performance of a research prototype CT scanner with small-pixel counting detector. Proceedings of SPIE--the International Society for Optical Engineering. 2013; 8668:86680O.
22. Yu Z, , et al. SPIE Medical Imaging. International Society for Optics and Photonics; 2016. Low-dose performance of a whole-body research photon-counting CT scanner.
23. Pourmorteza A, et al. Abdominal Imaging with Contrast-enhanced Photon-counting CT: First Human Experience. Radiology. 2016; 279(1):239–245. [PubMed: 26840654]
24. Symons R, et al. Photon-Counting Computed Tomography for Vascular Imaging of the Head and Neck: First In Vivo Human Results. Invest Radiol. 2018; 53(3):135–142. [PubMed: 28926370]
25. Leng S, et al. Dose-efficient ultrahigh-resolution scan mode using a photon counting detector computed tomography system. Journal of Medical Imaging. 2016; 3(4):043504–043504. [PubMed: 28042589]
26. Leng S, et al. Ultra-High Spatial Resolution, Multi-Energy CT using Photon Counting Detector Technology. Proceedings of SPIE--the International Society for Optical Engineering. 2017 NIH Public Access.
27. Mannil M, et al. Photon-Counting CT: High-Resolution Imaging of Coronary Stents. Invest Radiol. 2018; 53(3):143–149. [PubMed: 28945655]
28. Yu Z, et al. How Low Can We Go in Radiation Dose for the Data-Completion Scan on a Research Whole-Body Photon-Counting Computed Tomography System. Journal of computer assisted tomography. 2016; 40(4):663–670. [PubMed: 27096399]
29. Leng S, et al. A high-resolution imaging technique using a whole-body, research photon counting detector CT system. Proceeding of SPIE Medical Imaging. 2016; 97831
30. Stierstorfer K, et al. Weighted FBP--a simple approximate 3D FBP algorithm for multislice spiral CT with good dose usage for arbitrary pitch. Phys Med Biol. 2004; 49(11):2209–18. [PubMed: 15248573]
31. Flohr TG, et al. Novel ultrahigh resolution data acquisition and image reconstruction for multi-detector row CT. Med Phys. 2007; 34(5):1712–23. [PubMed: 17555253]
32. McCollough CH, et al. Spatial resolution improvement and dose reduction potential for inner ear CT imaging using a z-axis deconvolution technique. Med Phys. 2013; 40(6):061904. [PubMed: 23718595]
33. Leng S, et al. Temporal Bone CT: Improved Image Quality and Potential for Decreased Radiation Dose Using an Ultra-High-Resolution Scan Mode with an Iterative Reconstruction Algorithm. AJNR Am J Neuroradiol. 2015; 36(9):1599–603. [PubMed: 25999413]
34. Baek J, Pineda AR, Pelc NJ. To bin or not to bin? The effect of CT system limiting resolution on noise and detectability. Physics in medicine and biology. 2013; 58(5):1433. [PubMed: 23399724]
35. Kakinuma R, et al. Ultra-high-resolution computed tomography of the lung: image quality of a prototype scanner. PloS one. 2015; 10(9):e0137165. [PubMed: 26352144]

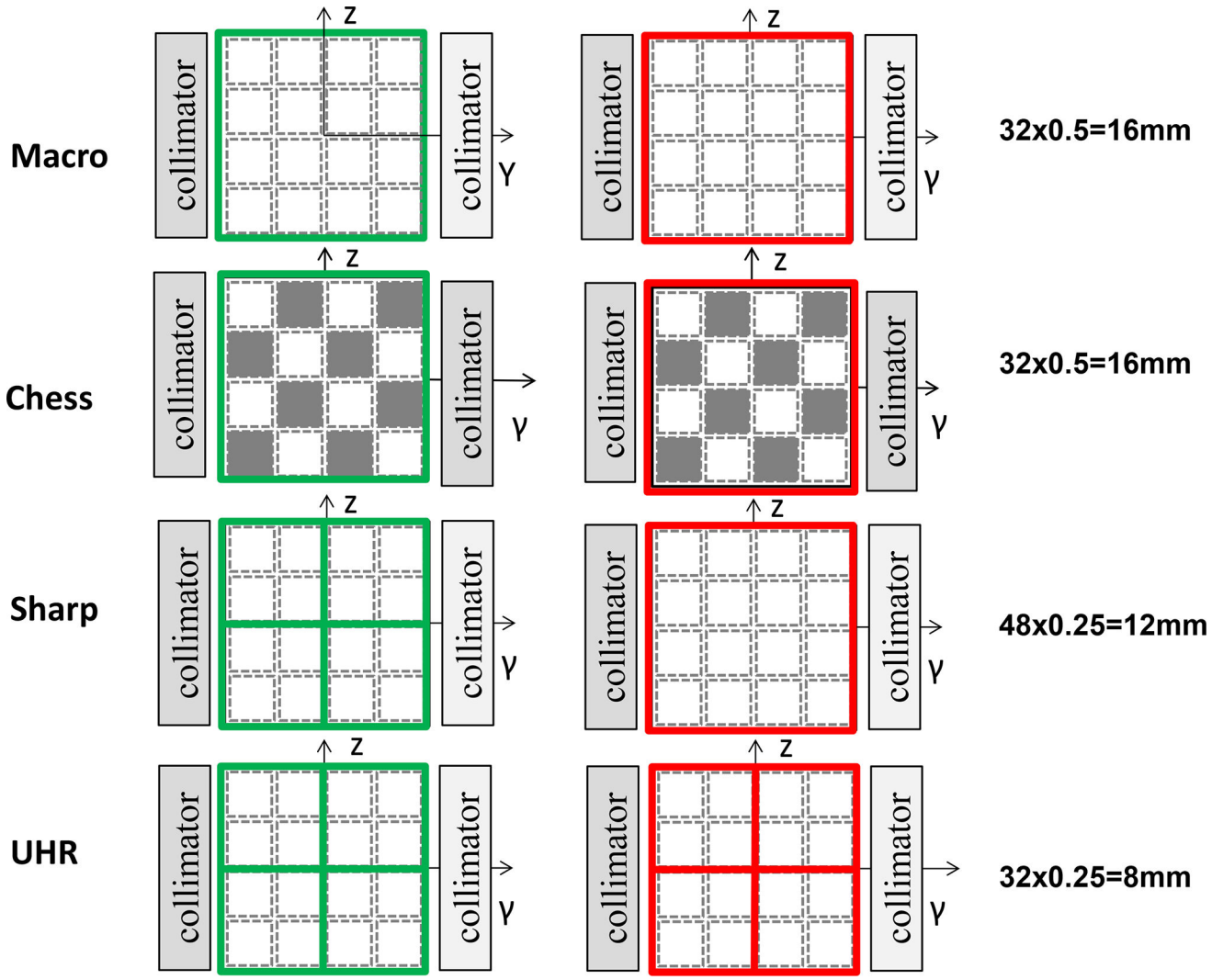

Figure 1.

Detector pixel configuration and z-axis collimation for the 4 scans modes on the PCD-CT system: *Macro*, *Chess*, *Sharp* and *UHR*. Native detector pixels are delineated by the dashed lines while detector readout units are delineated by solid lines for the low energy (green) and high energy (red) data.

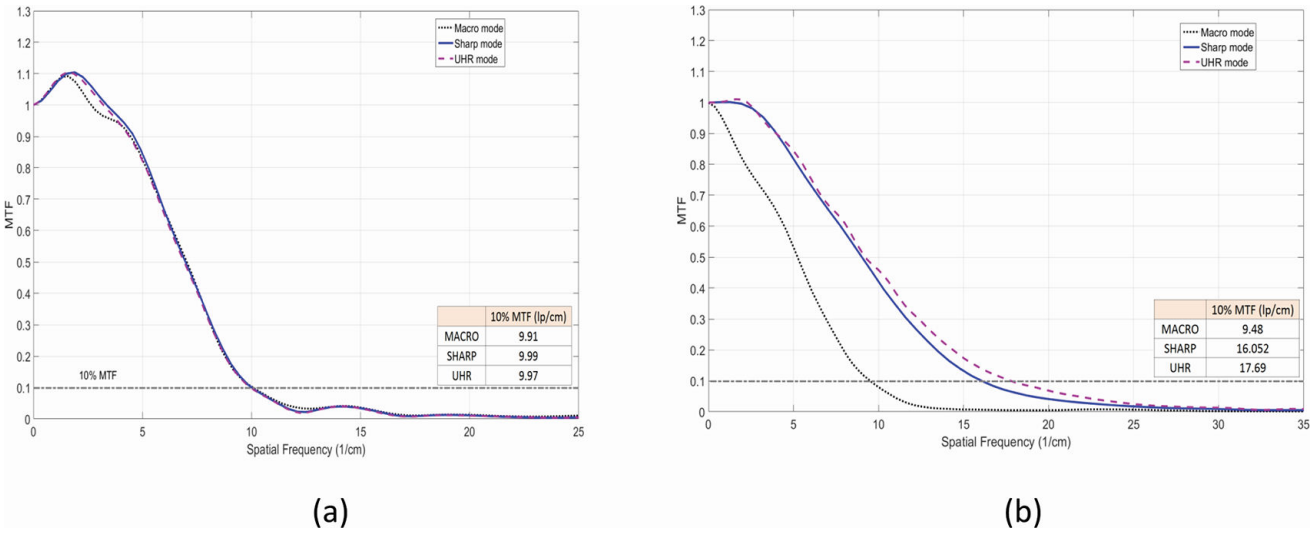

Figure 2.

MTF curves and corresponding 10% MTF values for Macro, Sharp and UHR modes with images reconstructed with B70 kernel (a) and S80 kernel (b).

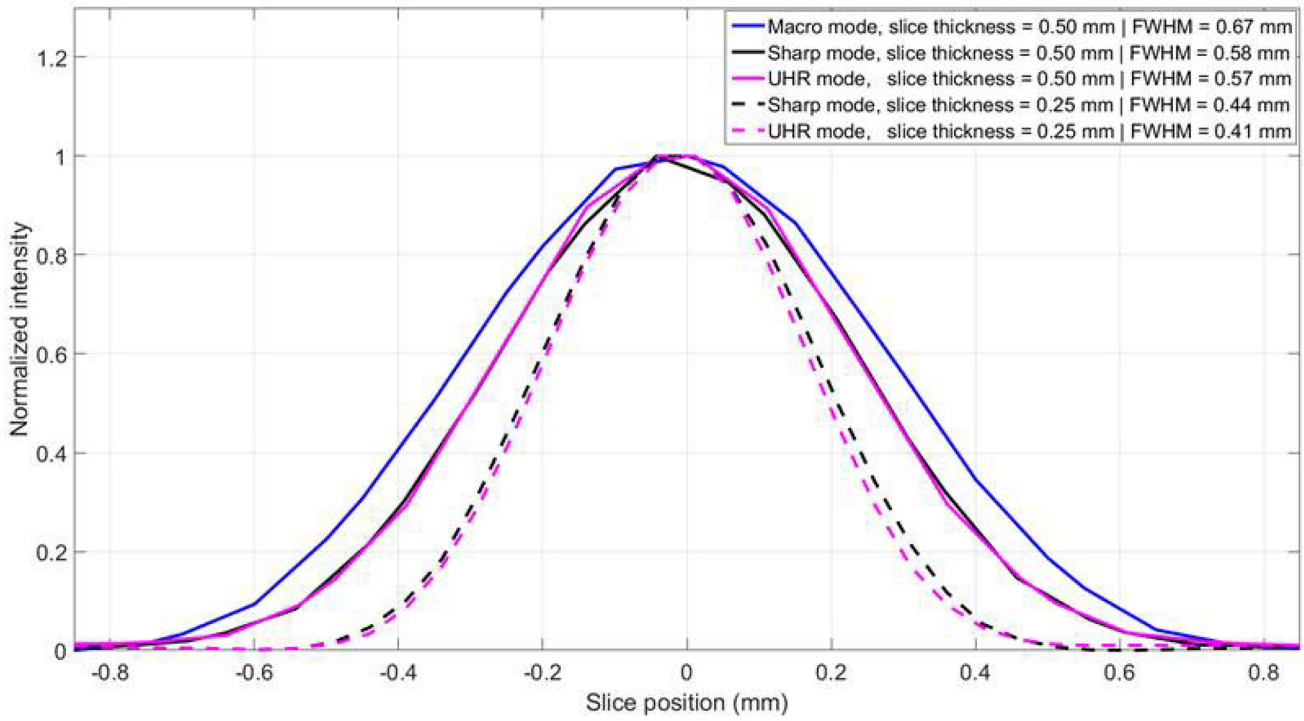

Figure 3.

SSPs of Macro, Sharp and UHR images reconstructed at 0.5 and 0.25 mm slice thickness, with corresponding FWHM of each SSP labeled.

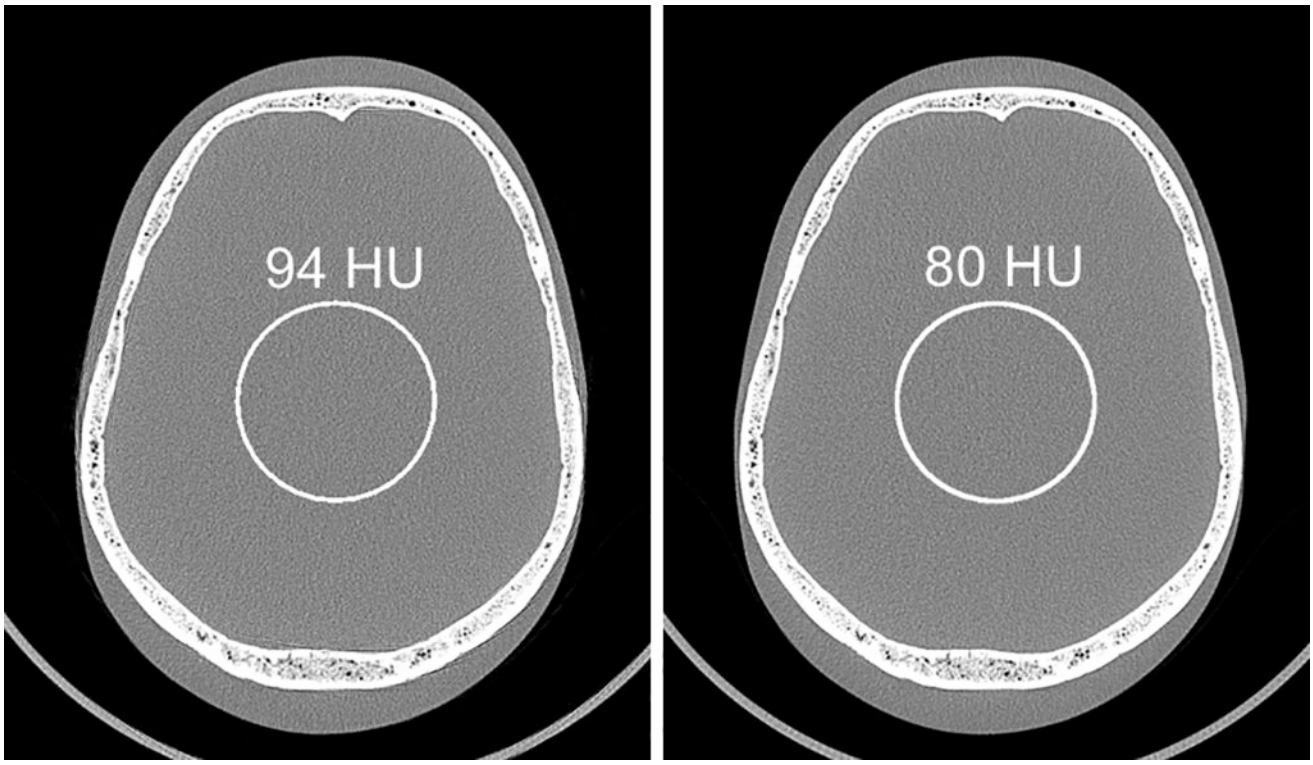

Figure 4.

Images of an anthropomorphic head phantom scanned with Macro (a) and Sharp (b) modes and reconstructed with the same head kernel. Noise measurements showed 15% noise reduction (from 94 to 80 HU) using *Sharp* mode compared to *Macro* mode.

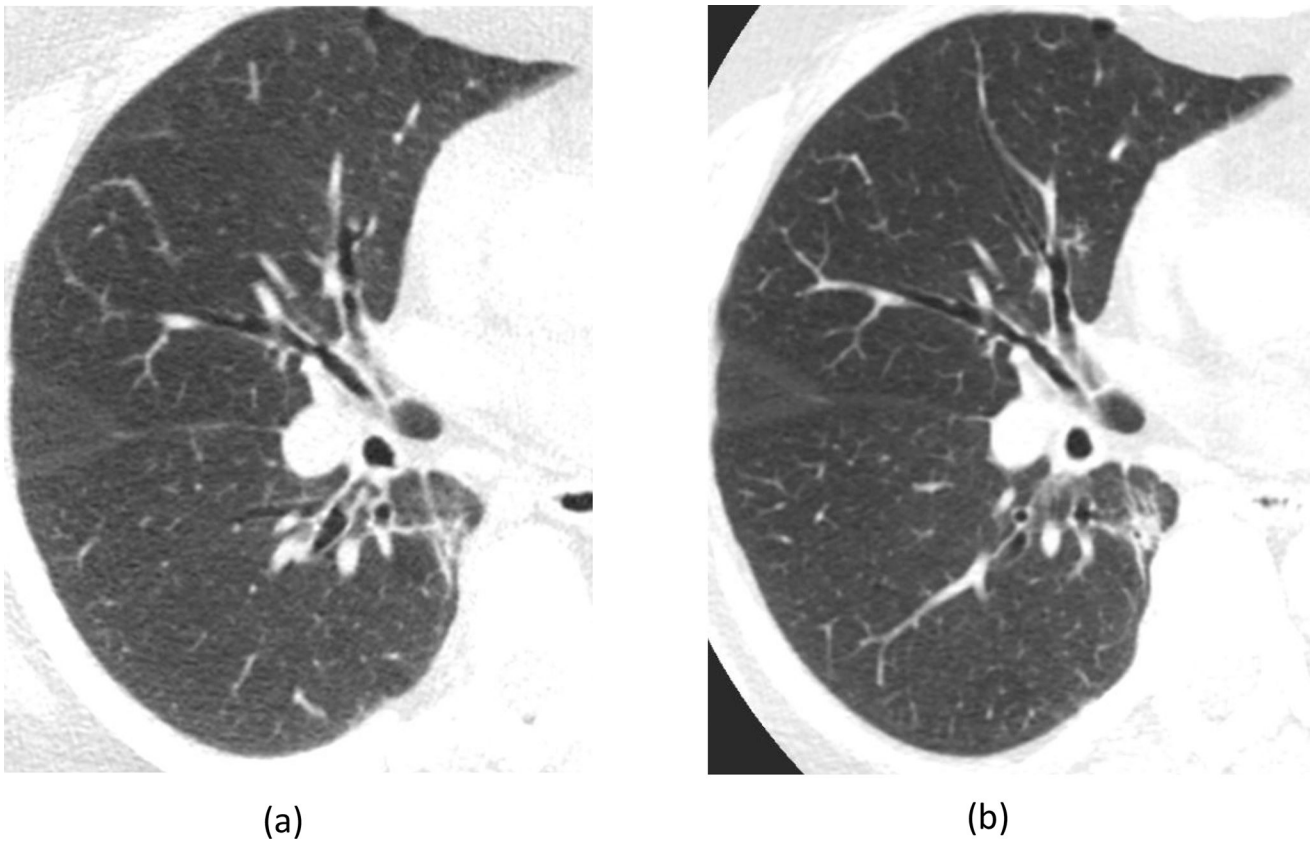

Figure 5.

Lung images from the same patient scanned on an EID-CT (a) and the PCD-CT (b). Image locations were selected to be as similar as possible. Compared to EID-CT, the PCD-CT image was much sharper, with excellent airway wall delineation and more small vessels observed.

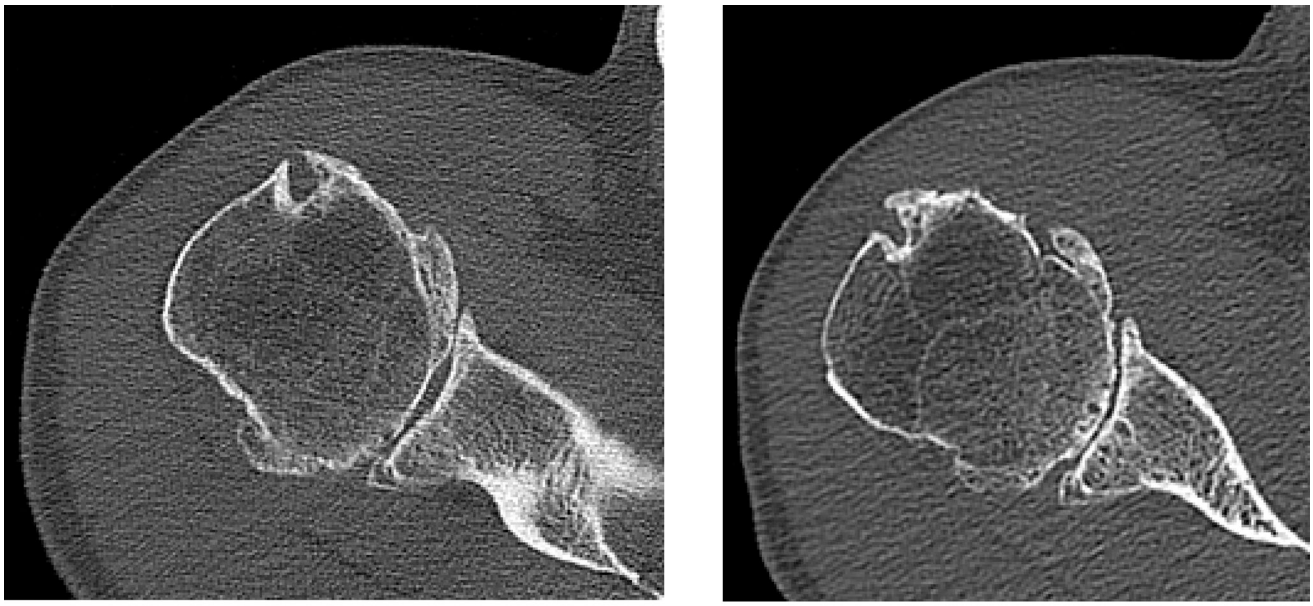

Figure 6.
Shoulder images from the same patient scanned on an EID-CT (a) and the PCD-CT (b). Image locations were selected to be as similar as possible. The PCD image shows sharper cortex and trabecular bone, and subchondral cysts and sclerosis compared to the EID image.

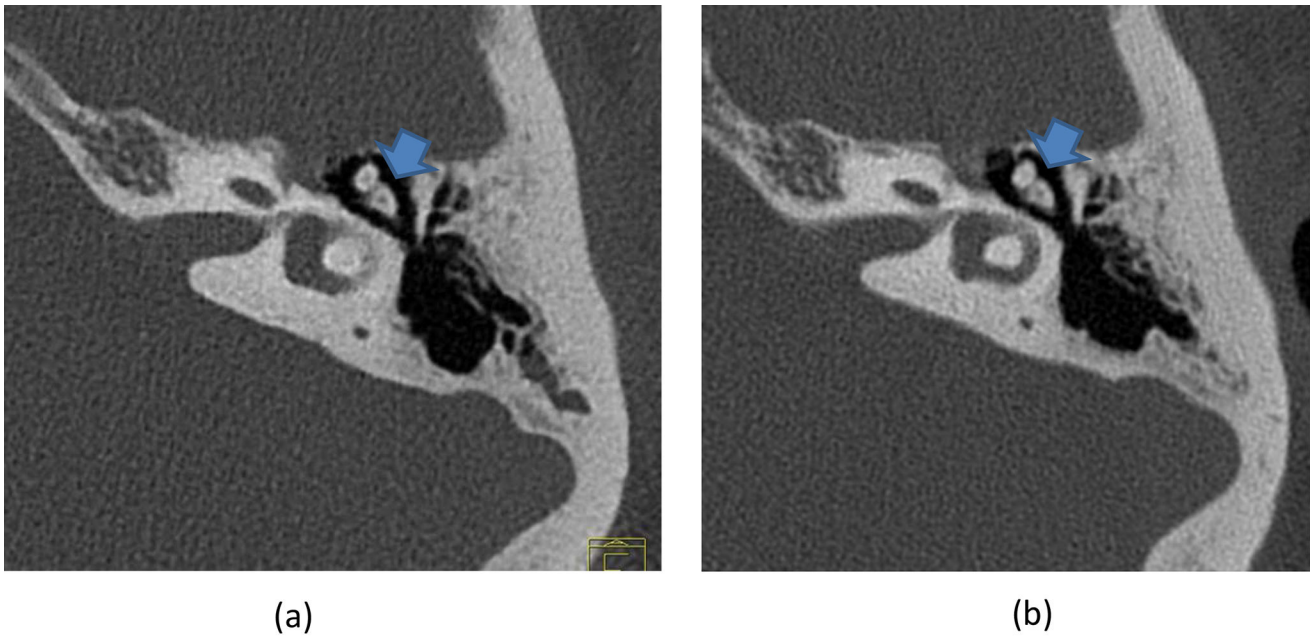

Figure 7.

Temporal bone images show high spatial resolution and clear delineation of the incudomallear joint (arrow) for both EID-CT (a) and PCD-CT (b). However, measurements showed a 21% noise reduction (141 to 112 HU) for PCD-CT compared to EID-CT, which uses a dose-inefficient comb filter to decrease the effective detector pixel sizes.

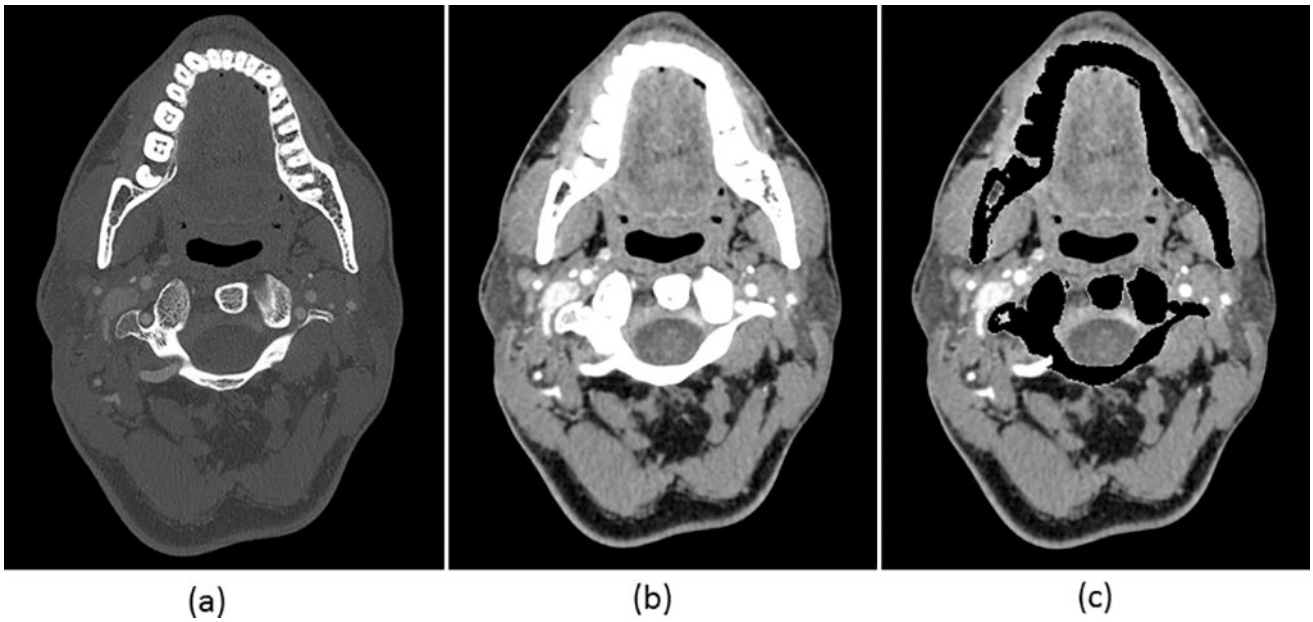

Figure 8.

Images from a single head CTA exam using PCD-CT can provide both a high spatial resolution single energy image (a), and a dual-energy processed image before (b) and after bone removal (c). Display settings: W/L = 1800/400 HU bone window for (a), W/L = 40/300 HU soft tissue window for (b) and (c).

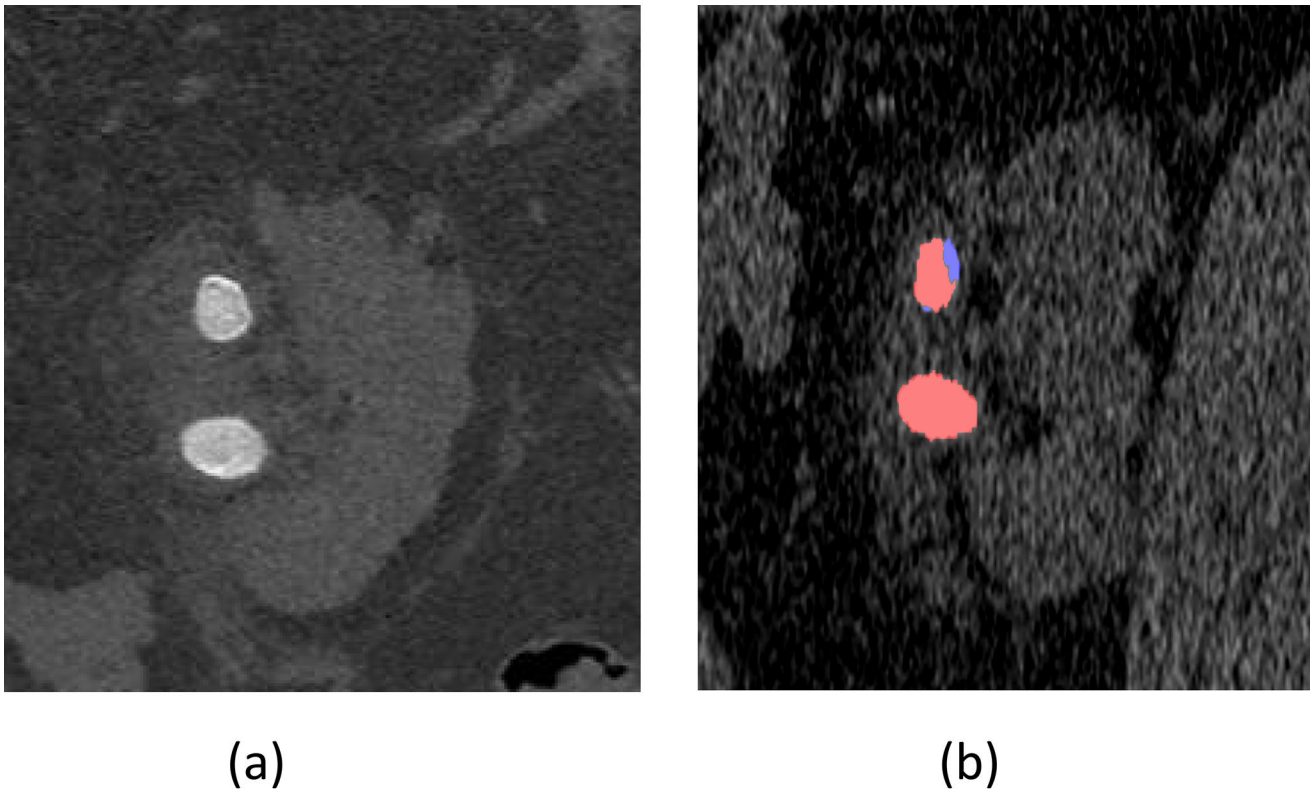

Figure 9.
The low-energy threshold image demonstrates sharp boundaries of the stone (a). The dual-energy post-processed image (b) demonstrates a pure uric acid stone (red) and a mixed stone with both uric acid (red) and non-uric-acid (blue) components.

Table 1

Scanning and reconstruction parameters for the *in vivo* patient studies.

	Lung		Shoulder		Temporal Bone		Head CTA	Renal Stone
Scanner Model	**Flash**	**CounT**	**Edge**	**CounT**	**Flash**	**CounT**	**CounT**	**CounT**
Scan Mode	**Single Energy**	**Sharp**	**Single Energy**	**Sharp**	**UHR w/ Comb Filter**	**UHR**	**Sharp**	**Sharp**
Collimation (mm)	128×0.6	48×0.25	128×0.6	48×0.25	16×0.6	32×0.25	48 ×0.25	48×0.25
Rotation time (s)	0.5	0.5	1	1	1	1	0.5	0.5
Tube potential (kV)	120	140	140	140	120	140	140	140
Effective mAs	228	126	142	120	420	207	190	146
$CTDI_{vol}$ (mGy)	15.4	15.3	14.6	14.5	58.0	57.5	52.1	17.7
Reconstruction Parameters								
Kernel	B46	B46	B70	B70	V80	V80	U71/D30	B46/D30
FOV	275	275	275	275	150	150	275	275
Slice thickness	1.5	1.5	0.6	0.6	0.5	0.5	0.6	0.25